ELSEVIER

Ultrasound in Med. & Biol., Vol. ■, No. ■, pp. 1–11, 2016

0301-5629/$ - see front matter

http://dx.doi.org/10.1016/j.ultrasmedbio.2016.05.013

● *Original Contribution*

COMPLEMENTARY DETECTION OF MULTIPLE ELECTRICAL SOURCES IN TISSUE USING ACOUSTOELECTRIC EFFECTS

ZHAOHUI WANG,* RAJAB CHALLOO,* HU PENG,† CHUNG S. LEUNG,* and RUSSELL S. WITTE‡§¶

*Department of Electrical Engineering and Computer Science, Texas A&M University—Kingsville, Kingsville, Texas, USA; †Department of Biomedical Engineering, School of Medical Engineering, Hefei University of Technology, Hefei, Anhui, China; ‡Department of Optical Sciences, University of Arizona, Tucson, Arizona, USA; §Department of Biomedical Engineering, University of Arizona, Tucson, Arizona, USA; and ¶Department of Medical Imaging, University of Arizona, Tucson, Arizona, USA

(*Received* 26 *November* 2015; *revised* 8 *May* 2016; *in final form* 16 *May* 2016)

Abstract—Accurate 3-D mapping of multiple bioelectric sources in nerve fibers with high spatial resolution is challenging for the diagnosis and treatment of a variety of neural abnormalities. Ultrasound current source density imaging exploits the acoustoelectric (AE) effect, an interaction between electrical current and acoustic pressure waves propagating through a conducting material, and has distinct advantages over conventional electrophysiology (*i.e.*, without ultrasound) for mapping electrical current flow in tissue. Ultrasound current source density imaging and two complementary Wheatstone bridge circuits were used to simultaneously detect two separate current flows induced in tissue phantoms. It has been found that the addition and subtraction of AE signals acquired by two circuits are independent components, regardless of whether the two sources are positioned at the same or different depths. In the ultrasound field, the AE signal from the bridge circuits is stronger, with a higher signal-to-noise ratio, than without a bridge circuit. Both experimental and simulated AE images depend on the magnitude and direction of the current, as well as the geometry (shape and thickness) and location of the current sources in the ultrasound field (2.25-MHz transducer). The experimental results are consistent with simulations consisting of multiple current sources. Real-time 3-D ultrasound current source density images of multiple current flows co-registered with convention pulse echo ultrasound potentially facilitate monitoring of neurologic disorders. (E-mail: zhaohui.wang@tamuk.edu) **© 2016 World Federation for Ultrasound in Medicine & Biology.**

Key Words: **Acoustoelectric, Bioelectric, Electrophysiology, Mapping, Electroencephalography.**

INTRODUCTION

Three-dimensional mapping of bioelectric sources in the body with a high spatial resolution is important for the diagnosis and treatment of a variety of cardiac and neurologic disorders. Mapping of electrical sources has many applications in biomedical research. Electrical impedance tomography applies currents through electrodes attached to the surface of the body and measures the resulting voltages to reconstruct approximate pictures of the electric conductivity inside the body (Cheney et al. 1999). In magnetoacousto-tomography (Towe and Islam 1988), the electrical current in biological tissue that was placed in a vibrating magnetic field generates acoustic vibrations inside the tissue volume because of the Lorentz force. Acoustic signals are then measured around the object for inverse reconstruction. The conductivity distribution of head–brain tissue is reconstructed by considering the charge accumulating at the interfaces. Wen et al. (1998) thought that this imaging method was based on the classic Hall effect, but Roth and Wikswo (1998) disagreed and claimed that the Hall effect was not involved in this technique.

In magnetoacousto-tomography with magnetic induction (Xu and He 2005), instead of using electrical stimulation, the eddy current induced in the tissue by a time-varying magnetic field interacts with the static magnetic field to create acoustic vibrations. In magnetic resonance electrical impedance tomography (Kwon and Woo 2002), a small current is injected into the object to be imaged through a pair of surface electrodes, and the magnetic flux density inside the object is measured with a magnetic resonance imaging scanner. This imaging technique can non-invasively reconstruct the static image of a conductivity distribution within an object.

Address correspondence to: Zhaohui Wang, Department of Electrical Engineering and Computer Science, Texas A&M University—Kingsville, MSC 192, 700 University Boulevard, Kingsville, TX 78363, USA. E-mail: zhaohui.wang@tamuk.edu

In magnetoacousto-electrical tomography (Haider et al. 2008), an ultrasonic pulse is focused on the sample that is placed in a static magnetic field to simulate a point-like current dipole source at the focal point because the vibration of the tissues inside the field induces an electrical current by the Lorentz force. Based on the reciprocity theorem, the voltage/current signal is proportional to a component of the lead field current density in volume conductors.

Grasland-Mongrain et al. (2013) proposed a similar method, Lorentz force electrical impedance tomography, to image the electrical conductivity of biological tissues through their sonication in a magnetic field: vibration of the tissues inside the field induces an electrical current by the Lorentz force. The current, detected by electrodes placed around the sample, is proportional to the ultrasonic pressure, to the strength of the magnetic field and to the electrical conductivity gradient along the acoustic axis. By focusing on different places inside the sample, a map of the electrical conductivity gradient can be established.

Three-dimensional ultrasound current source density imaging (UCSDI) (Olafsson et al. 2007) potentially overcomes the limitations of conventional electrophysiology (*i.e.*, no ultrasound) by providing enhanced spatial resolution, as determined by the ultrasound focus, combined with fewer invasive detection schemes (Wang et al. 2011). The voltage signal between two recording electrodes can be detected with a higher signal-to-noise ratio (SNR) by UCSDI according to Ohm's law and the acoustoelectric (AE) effect.

The AE effect (Fox et al. 1946; Lavandier et al. 2000) is the interaction between a propagating acoustic wave and charged particles in a material (saline solution, gel, graphite, metal, *etc*.). Acoustoelectric tomography (Zhang and Wang 2004), following the same principles as UCSDI, images the electric impedance properties of biological tissue with high spatial resolution; the contrast is determined by the electrical impedance, medium-dependent modulation coefficient and acoustic properties. The detected AE signal is proportional to the applied pressure and current density and is sensitive to the direction of current flow (Wang and Witte, 2014).

Neural disorders, such as arrhythmia in the heart and epilepsy in the brain, could greatly benefit from this new diagnostic tool that non-invasively maps conduction in abnormal tissue. UCSDI had been used to quickly map cardiac activation waves in live rabbit hearts, and the conduction velocity of the heart estimated from the shifts was 0.25 ± 0.05 mm/ms (Olafsson et al. 2006, 2009). Therefore, ultrasound with a speed of approximately 1540 mm/s is fast enough to image the neuronal pulse signal. To overcome the limitation of the weak AE signal associated with the electrocardiogram, the effects of the electrode configuration and ultrasound frequency on the magnitude of the AE signal and quality of UCSDI were also investigated using a rabbit Langendorff heart model (Qin et al. 2015). It was found that the AE signal was much stronger at 0.5 MHz than at 1.0 MHz, and a clinical lasso catheter placed on the epicardium exhibited excellent sensitivity without penetrating the tissue.

Tracking different pathways of multiple intertwined nerve fibers is still a challenging topic for the diagnosis of cardiac and neural abnormalities. Electron micrographs that reflect density differences were used to analyze fine-structure nerve tissue, but they required ultrathin sectioning of the nervous tissue and fixative to avoid shrinkage and to produce the most delicate coagulum (Pease and Baker 2005). Diffusion tensor magnetic resonance imaging fiber tracking provides information about nerve connectivity, but this technique relies on the use of high-quality diffusion-weighted images and a suitable algorithm to generate the track. Additionally, its validation is not straightforward because of the lack of a gold standard (Tournier et al. 2002).

On the basis of the AE effect, two complementary bridge tissue circuits, each of which is similar to a Wheatstone bridge (Fig. 1a), are proposed here for the first time to simultaneously map multiple current flows induced in two conducting tissue phantoms positioned at various depths. They can detect the relative position of the two tissue phantoms transmitting current in different directions by applying simple addition and subtraction to the measured UCSDI.

In this study, the simulation of the AE signal, based on the lead theory (Malmivuo and Plonsey, 1995), was used to analyze the dimensional effects over sensitivity and frequency spectra. The proposed complementary circuit theory is provided in the Appendix and evaluated by *in silico* simulation, which is further compared with *in vitro* experiments using a single-element ultrasound transducer.

METHODS

The custom simulation program developed in MATLAB (The MathWorks, Natick, MA, USA) is based on ultrasound field and lead field theory using known properties of the ultrasound transducer and dielectric properties of the test phantoms to complement the experimental model and further characterize the relationship between the ultrasound beam and electrical properties of the tissue.

Acoustoelectric equations

In Figure 2a, the center of the transducer is $T(0, 0, 0)$, and the center of the tissue slab is $C(x_0, y_0, z_0)$. In the experiment, the phantoms are placed at the focus of the

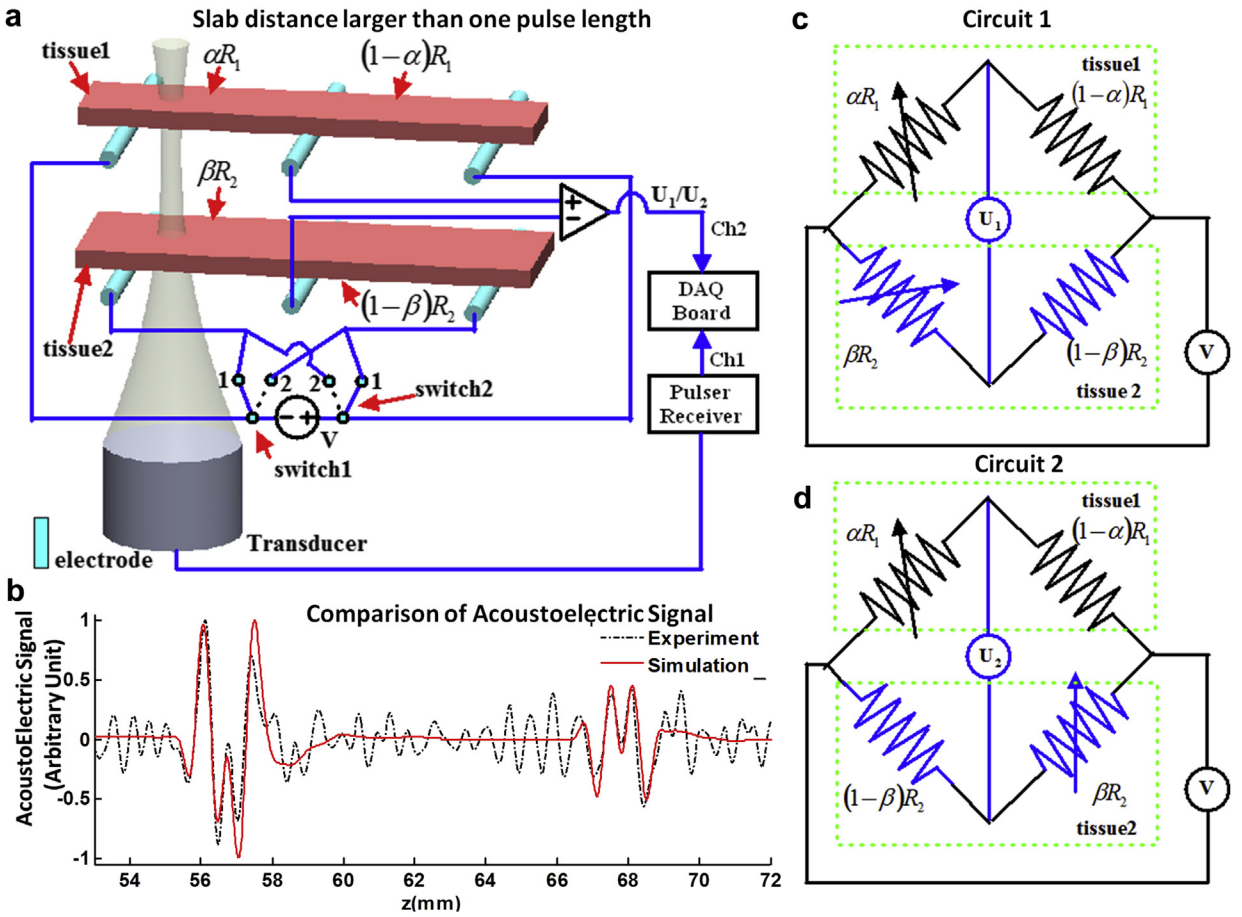

Fig. 1. Simulation and experimental setups for ultrasound current density imaging of two tissue slabs at a distance larger than one pulse length. (a) Two tissue slabs aligned horizontally at a distance larger than the length of one pulse. The switches are used for the complementary bridge circuits: position 1 for circuit 1, position 2 for circuit 2. The ultrasound modulates the electric field on the left segments from the bottom. (b) The simulated acoustoelectric signal (A-line) is compared with the acoustoelectric signal obtained in the experiment (a). (c) First case (circuit 1), when switches in (a) are set at position 1. (d) Second case (circuit 2), when switches are set at position 2.

transducer, $z_0 = z_f$, where z_f is the focal length. Any point P in the ultrasound pressure field (x, y, z) can be described in the electric coordinate system or lead field as $(x-x_0, y-y_0, z-z_0)$ or $\overrightarrow{CP} = \overrightarrow{TP} - \overrightarrow{TC}$. In the electric field, because of a distributed current source, $\mathbf{J}^I = \mathbf{J}^I(x, y, z)$, the scalar voltage V measured by a detector at (0, 0, 0) with a tissue slab at (x_0, y_0, z_0) can be expressed in the 3-D equation using reciprocal theory, given the assumption of far-field detection of the AE signal (Malmivuo and Plonsey, 1995):

$$\begin{aligned} V(x_0,y_0,t) &= \iiint \rho(x,y,z,t)(\mathbf{J}^L\cdot\mathbf{J}^I) \\ &\quad \times(x-x_0,y-y_0,z-z_0)dxdydz \\ &= \iiint(\mathbf{J}^L\cdot\mathbf{J}^I)\rho_0 dxdydz + \iiint(\mathbf{J}^L\cdot\mathbf{J}^I) \\ &\quad \times(-K_I\rho_0 p)dxdydz \end{aligned} \tag{1}$$

Here $\mathbf{J}^L(x, y, z)$ is the electric lead field due to the unit reciprocal current along the tissue slab between two detecting electrodes, and the injected current density is $\mathbf{J}^I = I\mathbf{J}^L(x, y, z)$, with I denoting the injected current. $\Delta\rho/\rho_0 = -K_I\Delta P$, where $\Delta\rho$ is the resistivity change, ρ_0 is the direct current resistivity, ΔP is the acoustic pressure and K_I is the interaction constant on the order of 10^{-9} Pa^{-1} in saline. $\rho = \rho(x, y, z, t) = \rho_0(1-K_I p)$ is the resistivity whose distribution is under the modulation of scalar ultrasound pressure $p = \Delta P$. Tensor $\mathbf{J}^L\cdot\mathbf{J}^I$ is the inner product between $\mathbf{J}^L$ and $\mathbf{J}^I$. In (1), V has a low-frequency component (first term) and a high-frequency component (second term), which is the useful AE signal V^{AE} (Olafsson et al. 2007).

For both simulated data and measured data, the AE signal V^{AE} is filtered by a bandpass filter around the center frequency of the transducer to achieve a higher SNR. Pressure $p(x, y, z, t)$ can be expanded into its subcomponents such that

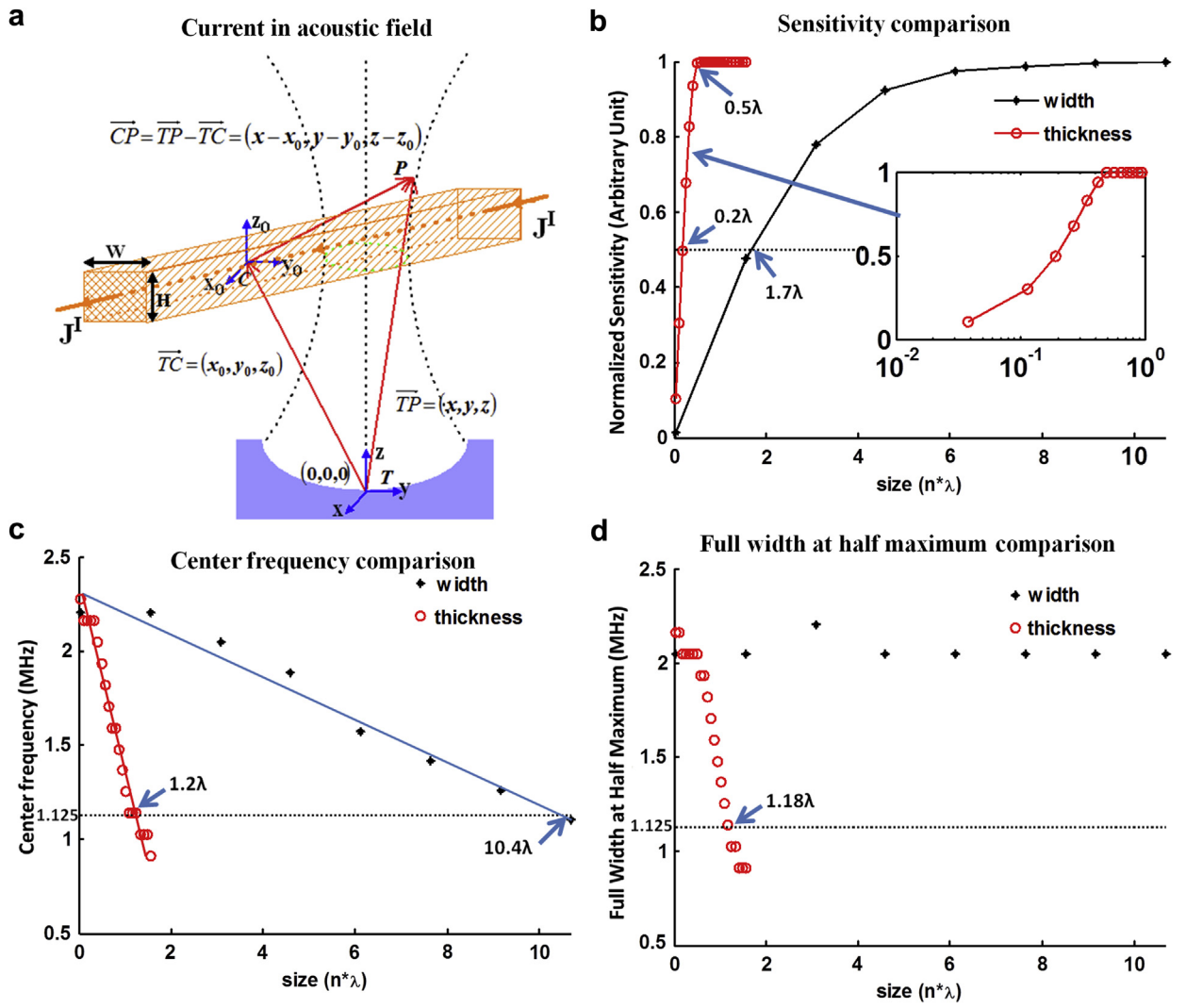

Fig. 2. Simulation configuration and results: The size of the tissue slab is analyzed by varying the thickness from $\lambda/25$ to λ and the width from $\lambda/25$ to 11λ. (a) Schematic of the acoustoelectric effect on the tissue slab. The transducer center is $T(0, 0, 0$, and $C(x_0, y_0, z_0)$ is at the center of the electric coordinate system or lead field. Any point P in the ultrasound pressure field (x, y, z) can be described in the electric field as $(x-x_0, y-y_0, z-z_0)$, or $\overrightarrow{CP} = \overrightarrow{TP} - \overrightarrow{TC}$. (b) Plot of sensitivity (normalized) approaching a saturation value that is related to the wavelength. The sensitivity reaches the half-maximum value at a thickness of 0.2λ and a width of $1.7\ \lambda$. The inset with a logarithmic scale of thickness better illustrates the thickness curve. The horizontal axis is the size of the width/thickness that is defined as the number of wavelengths. (c, d) Analyses of the center frequency and full width at half-maximum over the spectrum of the simulated acoustoelectric A-lines. The center frequency of the transducer is 2.25 MHz (wavelength $\lambda = 658\ \mu$m in water).

$$p(x,y,z,t) = P_0 b(x,y,z) a\left(t-\frac{z}{c}\right) \tag{2}$$

with the ultrasound beam pattern $b(x, y, z)$ defined with respect to the transducer at the origin, pressure pulse amplitude P_0, pulse waveform $a(t)$ and speed of sound c.

For AE effect simulation, it is assumed that the single-element 2.25-MHz concave transducer is excited by a pulse obtained from the signal generator, and then, the ultrasound pressure field $p(x, y, z, t)$ can be created by Field II simulation software (Jensen 1997; Jensen and Svendsen 1992). The impulse response to the transducer was obtained from the AE signal of a commercial Onda hydrophone (HGL-0200, Onda, Sunnyvale, CA, USA). The AE voltage V^{AE} measured by a tissue slab under the modulation of a transducer at coordinate (x_0, y_0, z_0) in the electric field can be expressed in three dimensions:

$$V^{AE}(x_0,y_0,t) = -P_0 \iiint K_I \rho_0 (\mathbf{J}^L \cdot \mathbf{J}^I)(x-x_0, y-y_0, z-z_0) \times \left[b(x,y,z) a\left(t-\frac{z}{c}\right)\right] dxdydz \tag{3}$$

As $K_I = K_I(x, y, z)$ and $\rho_0 = \rho_0(x, y, z)$ both depend on the material properties, they can be combined together with $\mathbf{J}^I(x, y, z)$ and $\mathbf{J}^L(x, y, z)$ so that

$$w(x,y,z) = K_I(x,y,z)\rho_0(x,y,z)I\left|\mathbf{J}^L(x,y,z)\right|^2 \quad (4)$$

According to eqn (3), $V^{AE}(x_0, y_0, t)$ involves three convolutions of $w(x, y, z)$ and $p(x, y, z, t)$, so the calculation of V^{AE} can be greatly sped up by applying an inverse 3-D Fourier transform of the product between the current density distribution and ultrasound field in the frequency domain.

$$\begin{aligned} V^{AE}(x_0,y_0,t) &= -\iiint w(x-x_0,y-y_0,z-z_0)p(x,y,z,t)dxdydz \\ &= -F^{-1}_{x_0,y_0,z_0}\left\{W(k_x,k_y,k_z)F_{k_x,k_y,k_z}[p(x,y,z,t)]\right\} \end{aligned} \quad (5)$$

where $z_0 = z_f$, $F^{-1}_{k_xk_yk_z}$ is the 3-D Fourier transform over (x, y, z), $F^{-1}_{x_0y_0z_0}$ is the 3-D inverse Fourier transform over (k_x, k_y, k_z) and W is the 3-D Fourier transform of $w(x, y, z)$. k_x, k_y and k_z are projections of the wavenumber k along the x, y and z axes, respectively. If the coordinate origin is changed from T to C, the convolutions become correlations, whose computation can be accelerated by an inverse 3-D Fourier transform of the product between W and the conjugate of $F_{k_xk_yk_z}$.

As the long tissue slab is uniform along the longitudinal direction (y), the simulated A-line V^{AE} can be obtained by applying the convolution of the ultrasound field over the current distribution in tissue along the x–z cross section.

Two complementary bridge circuits

The two complementary bridge circuits (Fig. 1c, d) are similar to the Wheatstone bridge, where the best detecting position of each branch is on the midpoint. If the axial distance between two tissue slabs in an ultrasound field is larger than one acoustic pulse length, the AE signals in each tissue slab can be detected and isolated when an ultrasound pulse passes through at different times using only the first bridge circuit. If the axial distance is smaller than one pulse length, the detected AE signals in two tissue slabs partially overlap, and it is impossible to separate them using one bridge circuit. Two complementary bridge circuits, however, can effectively isolate the AE signal of each source from the mixture.

In Figure 1c, αR_1 and βR_2 refer to the segments of tissue slabs 1 and 2 whose resistances are modulated with the ultrasound pressure; R_1 and R_2 are the constant resistances of the two tissue slabs. Addition and subtraction of the signals detected by two circuits can rebuild the AE signals in tissue slabs 1 and 2 individually. From the Appendix, when the ultrasound beam is located on the left two electrodes, the A-line is filtered by a bandpass filter with the same center frequency of the ultrasound; then,

$$\frac{u_1+u_2}{2} = v_\alpha, \quad \frac{u_1-u_2}{2} = -v_\beta, \quad (6)$$

where u_1, u_2, v_α and v_β are the AC components of U_1, U_2, V_α and V_β, respectively. V_α and V_β are the voltage drops caused by the ultrasound modulation on segments αR_1 and βR_2, respectively. U_1 and U_2 are the signals measured by the differential amplifier using the first and second circuits, respectively. v_α and v_β are two independent components because α and β are independent of each other.

When the ultrasound beam focuses on the right part of the slabs (Fig. 1d),

$$\frac{u_1+u_2}{2} = -v_{1-\alpha}, \quad \frac{u_1-u_2}{2} = v_{1-\beta}, \quad (7)$$

where u_1, u_2, $v_{1-\alpha}$ and $v_{1-\beta}$ are the AC components of U_1, U_2, $V_{1-\alpha}$ and $V_{1-\beta}$, respectively. $V_{1-\alpha}$ and $V_{1-\beta}$ are the voltage drops caused by the ultrasound modulation on segments $(1-\alpha)R_1$ and $(1-\beta)R_2$, respectively. $v_{1-\alpha}$ and $v_{1-\beta}$ are also two independent components.

From eqns (6) and (7), the AC component of the voltage drop on each segment can be reconstructed directly from the addition or subtraction of the filtered signals measured by two complementary bridge circuits. The reconstructed voltage drops on the two tissue slabs in the ultrasound pressure field are two independent components. Therefore, the two tissue slabs can be separated by two complementary circuits, even though they are at the same depth.

Experimental setup

Each plastic rack was modified by forming a rectangular hole with a width of 15 mm and length of 80 mm so that the ultrasound pulse could reach the nerve phantoms unimpeded. Steel electrodes, with a length of 30 mm and a radius of 0.5 mm, were arranged parallel to each other at a 5-mm interval on the surface of the rack. On the bottom of the mineral oil tank, one rectangular acoustic window was opened and covered with Mylar film to isolate the mineral oil from the de-ionized water (diH_2O) and to allow the transducer pulse to pass through to modulate the current on the nerve phantoms (Fig. 3a). The transducer was placed in the water beneath the mineral oil tank and moved along the x–y–z direction under the control of motors, providing the ultrasound pressure to the two conducting phantoms.

Two phantoms (turkey tissue slabs) were washed with 0.9% saline to remove bubbles from the surface and were then soaked in 0.9% saline for 1 h to allow the saline to enter. Direct current resistance of the tissue

phantoms was in the range 1 to 10 kΩ range. Phantoms were placed in contact with stainless steel electrodes in the rack and were positioned at different distances from the acoustic focus. The bottom tissue slab was fixed inside the oil tank, whereas the position of the top tissue slab could be variably adjusted. The tissues were aligned horizontally at the same or different depths and submerged in mineral oil and separated from the ultrasound transducer placed in diH_2O by an acoustic window. A plastic supporter was used to fix the tissue slab on the electrodes for the case of two tissue slabs separated by a distance larger than one pulse length; for a distance less than one pulse length, one layer of Mylar film was used to separate the two tissue slabs. Two turkey slices (cut into long, thin rectangles) were injected with different current levels determined by the resistance of each slice using a common voltage source (Agilent 33220A, Agilent Technology, Palo Alto, CA, USA).

To detect the AE signal, two complementary bridge circuits were used. The connections can be seen in Figure 1a. Each tissue slab was connected to three electrodes spaced 5 mm apart, with the center electrode on each phantom connected to a differential amplifier (Lecroy 1855DA, Lecroy, Santa Clara, CA, USA). Excited by a square-wave pulser/receiver (Olympus 5077PR, Olympus NDT, Waltham, MA, USA), a single-element focused transducer (2.25 MHz, f/1.8, focal length 70 mm) emitted one period short pulse and received the echo signal. The pulse length was approximately 0.66 mm. The AE signal of the two phantoms was measured by the differential amplifier, regardless of the distance between the two phantoms, and was amplified, high-pass filtered and captured by a 12-bit data acquisition board (PDA12A, Signatec, Newport Beach, CA, USA). The maximum (90°) or minimum (270°) current injection was synchronized with the data acquisition board and the pulser/receiver. Common mode noise can be reduced by subtracting two AE signals with opposite phases. In post-processing, the detected A-line AE signal was bandpass filtered with center frequency 2.25 MHz and cutoff frequencies of 0.3 and 5 MHz to increase the SNR.

$$\mathrm{SNR} = 20\log_{10}\frac{S}{N} \tag{8}$$

where S is a peak–peak value of the signal, and N is the peak–peak value of noise. The pressure on the focus of the ultrasound field was measured with the Onda hydrophone at approximately 258 kPa.

To verify whether the complementary bridge circuits can separate the AE signals on two tissue slabs at a distance less than one pulse length, Mylar plastic film was used to approximate this distance. The two tissue slabs, both 4 mm wide and 0.8 mm thick, were each stuck to one side of the Mylar film, so that the slabs were separated by 0.2 mm (the thickness of the Mylar film, shorter

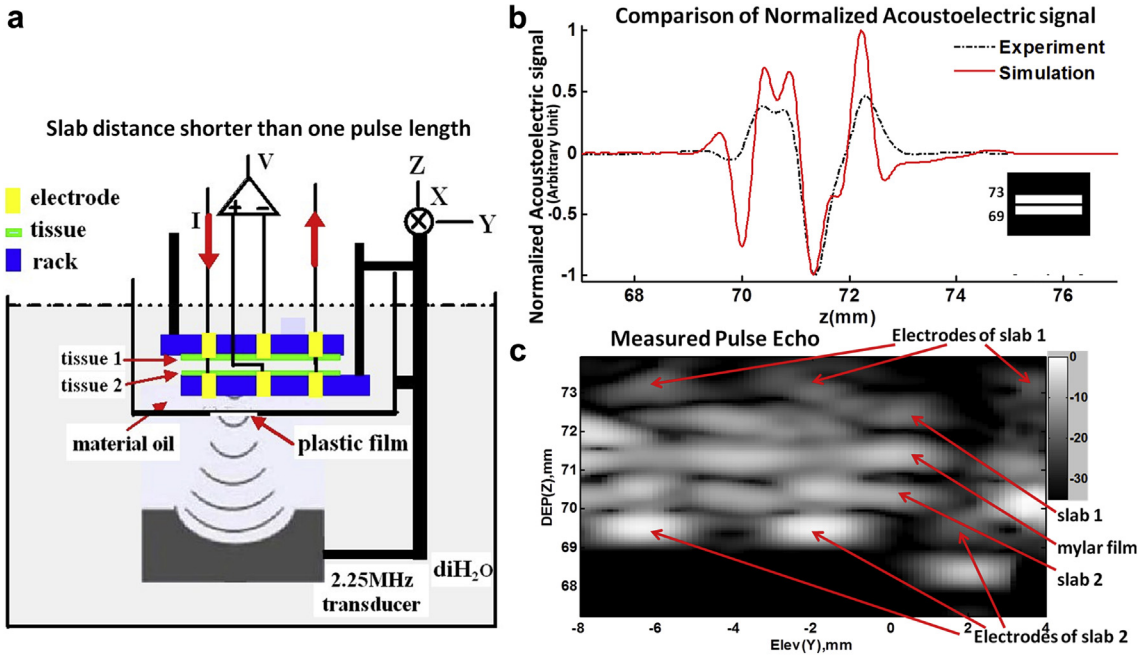

Fig. 3. Simulation and experimental setups for ultrasound current density imaging of two tissue slabs at a distance less than one pulse length. (a) Experimental setup of two tissue slabs in the mineral oil tank. (b) The radiofrequency signals obtained from experiment and simulation are measured at $x = 0$ mm and plotted in one axis. (c) Gray-scale pulse-echo image providing structural information on the experimental setup with a dynamic range of 35 dB.

than the acoustic pulse length, approximately 0.66 mm), and the currents through two tissues were set up according to the chosen bridge circuit. The Mylar film together with the tissue slabs was fixed between two racks (Fig. 3c). The 2.25-MHz transducer was moved from below along the *x*–*y* direction with 61 steps for 20 mm in each dimension to form 3-D AE + PE images.

Simulation

Simulation software for the AE effect was developed in MATLAB to complement the experimental model and further characterize the relationship between the ultrasound beam and electrical properties of the tissue. The simulation model had the same dimensions as the experimental phantom. The AE images from both the experiments and simulations depended on the magnitude and direction of the current, as well as the geometry (shape and thickness) and location of the current sources in the ultrasound field.

The simulation is based on the assumption of a constant current density and uniform distribution of the lead field $\mathbf{J}^{L}$ inside each tissue slab. The effect of width W of the tissue slab on the sensitivity spectrum was determined by changing W from 0.025 mm to 7.025 mm. The effect of thickness H of the tissue slab on the sensitivity spectrum was determined by changing H from 0.04λ to 0.5λ along the cross section with constant width. To compare the sensitivity–width and sensitivity–thickness curves in one plot, sensitivity was normalized against its maximum value with "arbitrary units."

RESULTS AND DISCUSSION

The long and thin tissue slab had a regular shape, with a uniform distribution of 0.9% saline made by long-term soaking, so the current density in the tissue slab can be considered to be uniformly distributed. A 3-D simulation of the tissue slab was also made in Multiphysics software (COMSOL, Palo Alto, CA, USA). For the boundary conditions of the electric current (3-D) module, different potentials were applied to the surfaces of the two ends, whereas the other surfaces were defined as "electric insulation." The simulation indicated that the current density distribution on the cross section was uniform. An ultrasound pulse was focused locally on the tissue slab in a very small area, modulating the local current density and enabling the AE signal to be detected. Scott et al. (1991) used nuclear magnetic resonance imaging to measure the electric current density in any substance and found that the current density outside the ping-pong sphere changed within small range.

Effect of size of the tissue slabs

Sensitivity depended on the amplitude of the bias current, as well as the width and thickness of the tissue slab. The simulations performed by Wang et al. (2010, 2013) illustrated that sensitivity was proportional to the thickness (within a half-wavelength) and width (within a beam diameter) of the tissue slab. When width W was changed from 0.025 to 7.025 mm, the peak positions of V^{AE} were maintained and the sensitivity reached a maximal value when the lateral width was larger than the beam size (Fig. 2b). When thickness H was changed from 0.04λ to 0.5λ, the V^{AE} amplitude increased linearly, whereas the thickness had an important effect on the spectrum of the AE signal. When the thickness increased from 0, the first harmonic magnitude decreased and reached the lowest value at thickness = 0.5λ (Fig. 2b); if the thickness was $>0.5\lambda$, the first harmonic began increasing and shifted to a lower frequency; if the thickness was larger than λ, the first harmonic component was lost, making the center frequency of the main lobe smaller (Wang et al. 2013).

According to Figure 2c, the center frequency of AE signals decreased with the increase in thickness (-9.08λ/MHz) faster than in width (-1.04λ/MHz). The ultrasound pulse transmitting through one medium convolved with the electric field, and the longer the period of convolution because of a larger thickness, the more the center frequency was shifted.

The full width at half-maximum (FWHM) of the bandwidth followed a different trend for slab width and thickness. The FWHM decreased with an increase in thickness. In Figure 2d, the FWHM was 2.05 MHz at $\lambda/2$ and 1.37 MHz at 1.03λ. However, the FWHM of the bandwidth did not change with width and was approximately 2.04 MHz at any width.

Two tissue slabs separated by more than one pulse length

The two tissue slabs separated by a distance larger than one pulse length (Fig. 1a) were easily differentiated when only the first bridge circuit was applied, so it was not necessary to use the second circuit. In Figure 1b, the AE signal provided high-quality structural information on the tissue, as the top and bottom surfaces of each slab were easily recognized; the pulse-echo (PE) signal did not reveal any information on the current. After the detected signal was filtered by a bandpass filter with the same center frequency as the ultrasound transducer, the noise signal exhibited frequency components similar to the AE signal.

Phantoms were simulated with properties similar to the real tissues, and the shape and amplitude of the simulated and measured AE signals were similar. In Figure 1b, the simulated AE signal (A-line) was

consistent with the AE signal obtained in the experiment, showing the same wave shape and peak position. The amplitude of the AE signals on the two surfaces of one tissue slab were much stronger than in the inner region. The two bottom peaks were approximately at 56.7 mm, while the two top peaks were located at 67.8 mm, consistent with the location of the surfaces of the tissue slabs. For the slab at 56.7 mm, the SNR is 24 dB.

Two tissue slabs separated by less than one pulse length

Data from two groups of 2-D scans were separately acquired by two complementary bridge circuits and were further used to create two new groups of data by addition and subtraction. In Figure 4, the hot color of the AE signals indicating the detected currents in the tissue slabs are superimposed on the gray PE ultrasound signals depicting structure. In Figure 4a, the top and bottom tissues were so close that three peaks were seen in the Y–Z image, whereas Figure 4b provides only residual or background signals. The two tissues were clearly separated in the images. In the reconstructed images, Figure 4c provides the sensing area of the top tissue; Figure 4d illustrates the two boundaries and the sensing areas of the bottom tissue, except that its relative position is slightly shifted upward. Therefore, 3-D UCSD images of current flow can be co-registered with anatomical (pulse-echo) ultrasound.

Acquired by the first circuit in the experiment and simulation (Fig. 5a, b), the AE signals on the bottom surface of the top slab and top surface of the bottom slab were mixed together, and the phase information on the middle two surfaces deviated strongly, while the complementary second bridge circuit provided additional phase information. In Figure 3b, both the simulation and experimental data indicate that the detected voltage was a mixture of two AE signals that partially overlapped at the interface between the two tissue slabs. In Figure 5c and d, after the addition and subtraction, the reconstructed AE signals reveal two distinct tissue slabs. For the measured data, the SNR of the AE signal for the first circuit is 50 dB, and for the second circuit, 13.8 dB; after computation, the SNR of the additional component is 40 dB, whereas for the subtracted component, it is 25.1 dB.

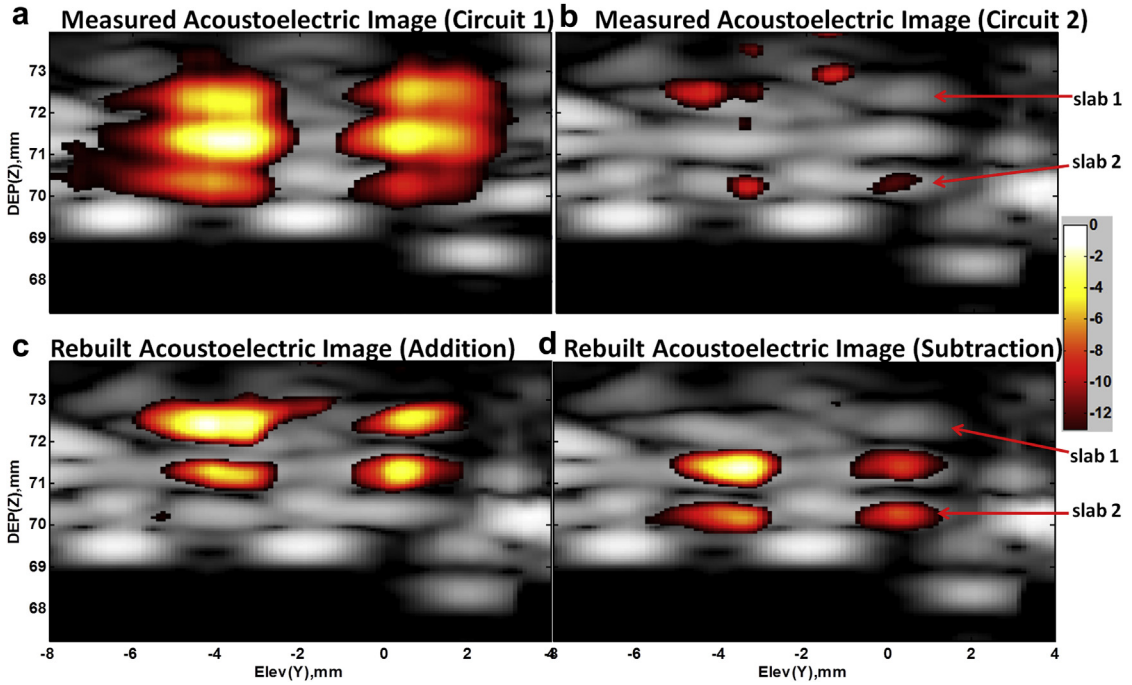

Fig. 4. Y-Z display of 3-D data of two tissue slabs on racks separated by a distance less than one pulse length. (a, b) Three-dimensional acoustoelectric data obtained from bridge circuit 1 and bridge circuit 2, respectively, by moving the 2.25-MHz transducer 61 × 61 steps in an area 20 × 20 mm from the bottom of tissue slabs. (c) Reconstructed 3-D images for the top tissue slab using addition. (d) Reconstructed 3-D images for the bottom tissue slab using subtraction. The acoustoelectric signal is displayed using a hot color map with a dynamic range of 13 dB, and the pulse-echo signal is overlaid using a gray color map with a dynamic range of 35 dB. The gray scale of the pulse-echo signal indicates the position of the tissue racks and slabs. The hot color of the acoustoelectric signal is the detected current and is co-registered and superimposed with the PE signal, which conveys structural information.

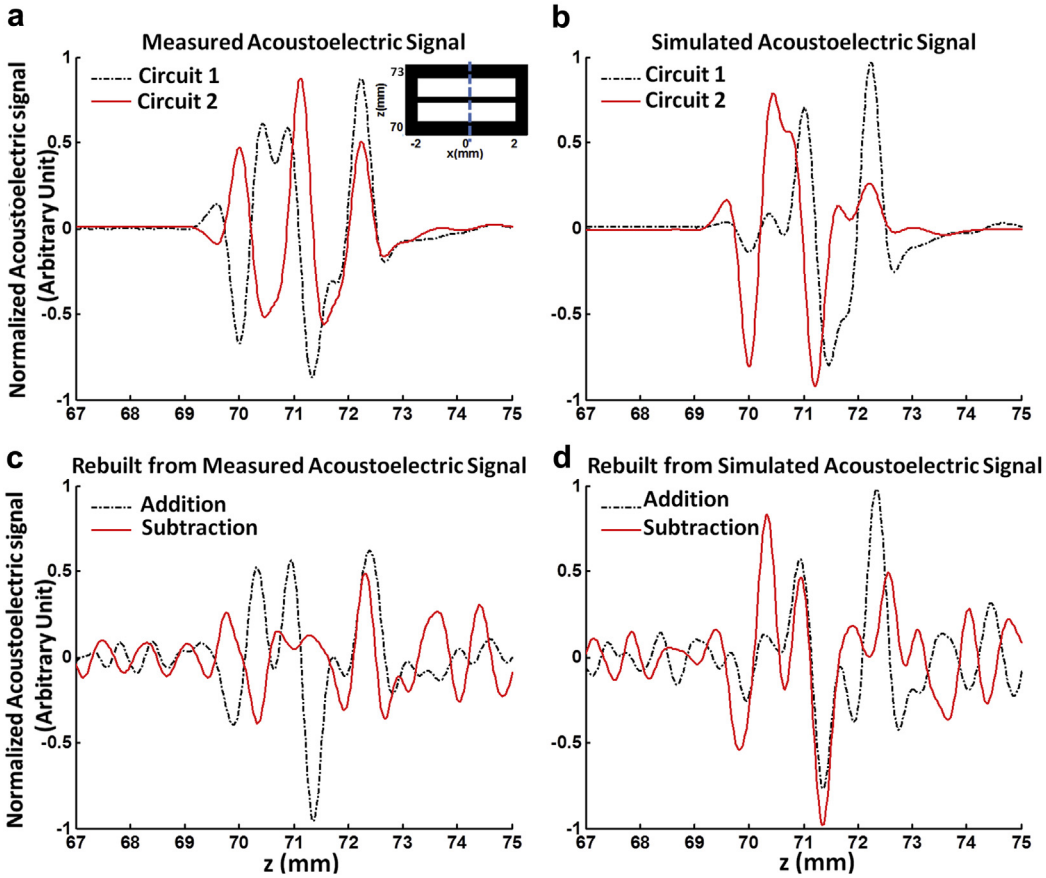

Fig. 5. Radiofrequency signals obtained from simulated and bench-top experiments using addition or subtraction for the two tissue slabs separated by less than one pulse length. (a) The two curves are the simulated radiofrequency signals through the lateral position at $x = 0.5$ mm for two complementary circuits. The inlet is the phantom for simulation, where the two nerve phantoms are both 4 mm wide and 0.8 mm thick and separated by 0.2 mm. (b) The two curves are the reconstructed radiofrequency signals from simulated data in (a) using addition or subtraction, respectively. (c) Radiofrequency signals measured by two complementary circuits at the point ($x = 0.5$, $y = -3.92$) mm in Figure 4. (d) Radiofrequency signals reconstructed from measured data using addition and subtraction.

Limitations and challenges

In the *in vitro* experiment, the current injected into the tissue was used to approximate the nerve signal (or action potential) propagation along the nerve axon. The nerve signal caused by the movement of sodium "ions" into the nerve cell generates current in one region that excites the neighboring region to generate an action potential. All of the action potentials generated by a single nerve cell are approximately the same shape and amplitude, regardless of the strength, duration or location of the stimulus that elicits them. The myelin sheath wrapping around the nerve axon is an electrical insulator, allowing faster and more energetically efficient conduction of impulses, making it possible to separate two nerve fibers using UCSDI. However, the ion flow in the current injected into tissue initially moves close to the speed of light, but deteriorates quickly over long distances.

The interaction constants of a saline-soaked turkey tissue and a nerve fiber are on the same order of 10^{-9} Pa^{-1} in saline. Li et al. (2012) reported that the K_I values in 0.9% saline and cardiac tissue are similar because physiologic saline contains 0.9% NaCl, which is approximately the salt concentration in extracellular fluid and blood. The AE effect was also found to be almost independent of concentration because the disassociation of the monovalent salt NaCl is essentially independent of concentration.

Temperature is not a major factor in ultrasound current source density imaging. The values of K_I at room temperature and physiologic temperature were similar (Li et al. 2012). The effect of temperature on K_I was examined from 2°C to 21°C in seawater, and no predictable trend was observed (Fox et al. 1946).

There are a few potential problems when applying this technology to clinical applications in nerve imaging, such as the signal strength, switched current and electrode contact on the nerve fibers. To differentiate two nerves at a distance less than one acoustic pulse length using the

complementary detection technique, one would need to wait until the current in one nerve fiber proceeds in one direction, then in an opposite direction. This switched current introduces two complementary signals that lead to a reconstruction of the AE signal in an individual nerve.

This technique requires three points on each fiber to map the whole nerve signal conduction path. However, for the case of unknown source locations, it is difficult to locate all three points on one fiber. Co-registered anatomical (pulse echo) ultrasound can help determine the positions of the recording electrodes by tracing from one end to the other two points on each branch. For the case of many intertwined nerve fibers, more delicate connections are required by separating fibers into multiple two-fiber groups, and each group outputs one differential AE signal. Co-registration of real-time 3-D UCSD images of multiple current flows with anatomical ultrasound potentially facilitates monitoring of neural abnormalities.

CONCLUSIONS

Three-dimensional mapping of bioelectric sources in the body using UCSDI can achieve higher spatial resolution than conventional electrical mapping without ultrasound. In this study, two complementary bridge circuits reduced common-mode noise and enabled AE signal detection with only two pairs of stainless steel recording electrodes and one pair of stimulating wires. This novel design can effectively distinguish two sources of currents in tissue no matter their proximity. By use of two complementary bridge tissue circuits to detect the ultrasound pressure, the branches of current flow in nerve phantoms can be simultaneously separated by applying simple addition and subtraction to UCSDI. These results are consistent with simulations consisting of multiple current sources. MATLAB simulations of tissue slabs provided accurate numerical solutions relating the measured voltage to the field current density and the displacement velocity induced by ultrasound. Both experimental and simulated UCSD images depended on the magnitude and direction of the current, as well as the geometry (shape and thickness) and location of the current sources in the ultrasound field. The experimental and analytical model described in this study provides a platform for developing multidimensional imaging of current flow based on UCSDI.

Acknowledgments—This study was supported by grants from the National Institutes of Health (R01EB009353) and Technology and Research Initiative Fund (TRIF).

REFERENCES

Cheney M, Isaacson D, Newell JC. Electrical impedance tomography. SIAM Rev 1999;41:85–101.

Fox FE, Herzfeld KF, Rock GD. The effect of ultrasonic waves on the conductivity of salt solutions. Phys Rev 1946;70:329–339.

Grasland-Mongrain P, Mari JM, Chapelon JY, Lafon C. Lorentz force electrical impedance tomography. Innovation Res Biomed Eng 2013;34:357–360.

Haider S, Hrbek A, Xu Y. Magneto-acousto-electrical tomography: A potential method for imaging current density and electrical impedance. Physiol Meas 2008;29:S41–S50.

Jensen JA. Field: A program for simulating ultrasound systems. Med Biol Eng Comp 1997;34:351–353.

Jensen JA, Svendsen NB. Calculation of pressure fields from arbitrarily shaped, apodized, and excited ultrasound transducers. IEEE Trans Ultrason Ferroelectr Freq Control 1992;39:262–267.

Kwon O, Woo EJ. Magnetic resonance electrical impedance tomography (MREIT): Simulation study of J-substitution algorithm. IEEE Trans Biomed Eng 2002;49:160–167.

Lavandier B, Jossinet J, Cathignol D. Quantitative assessment of ultrasound-induced resistance change in saline solution. Med Biol Eng Comput 2000;38:150–155.

Li Q, Olafsson R, Ingram P, Wang ZH, Witte RS. Measuring the acoustoelectric interaction constant using ultrasound current source density imaging. Phys Med Biol 2012;57:5929–5941.

Malmivuo J, Plonsey R. Bioelectromagnetism: Principles and applications of bioelectric and biomagnetic fields. New York: Oxford University Press; 1995.

Olafsson R, Witte RS, Huang SW, O'Donnell M. Ultrasound current source density imaging. IEEE Trans Biomed Eng 2007;50:1840–1848.

Olafsson R, Witte RS, Jia CX, Huang SW, Kim K, O'Donnell M. Cardiac activation mapping using ultrasound current source density imaging (UCSDI). IEEE Trans Ultrason Ferroelectr Freq Control 2009;56:565–574.

Olafsson R, Witte RS, Kim K, Ashkenazi S, O'Donnell M. Electric current mapping using the acousto-electric effect. In: Emelianov S, Walker WF, (eds). Medical Imaging 2006: Ultrasonic Imaging and Signal Processing. Proc SPIE 2006;6147;. p. 61470O.

Pease DC, Baker RF. Electron Microscopy of nervous tissue. Anat Rec 2005;110:505–529.

Qin YX, Li Q, Ingram P, Barber C, Liu ZL, Witte RS. Ultrasound current source density imaging of the cardiac activation wave using a clinical cardiac catheter. IEEE Trans Biomed Eng 2015;62:241–247.

Roth BJ, Wikswo JP. Comments on "Hall Effect Imaging". IEEE Trans Biomed Eng 1998;45:1294–1295.

Scott GC, Joy MLG, Armstrong RL, Henkelman RM. Measurement of nonuniform current density by magnetic resonance. IEEE Trans Med Imaging 1991;10:362–374.

Tournier JD, Calamante F, King MD, Gadian DG, Connelly A. Limitations and requirements of diffusion tensor fiber tracking: An assessment using simulations. Magn Reson Med 2002;47:701–708.

Towe BC, Islam MR. A magneto-acoustic method for the noninvasive measurement of bioelectric currents. IEEE Trans Biomed Eng 1988;35:892–894.

Wang ZH, Ingram P, Olafsson R, Greenlee C, Norwood R, Witte RS. Simulation-based optimization of the acoustoelectric hydrophone for mapping an ultrasound beam. Proc SPIE 2010;7629:76290Q.

Wang ZH, Ingram P, Olafsson R, Greenlee C, Norwood R, Witte RS. Design considerations and performance of MEMS acoustoelectric ultrasound detector. IEEE Trans Ultrason Ferroelectr Freq Control 2013;60:1906–1916.

Wang ZH, Olafsson R, Ingram P, Li Q, Witte RS. Four-dimensional ultrasound current source density imaging of a dipole field. Appl Phys Lett 2011;99:113701.

Wang ZH, Witte RS. Simulation based validation for four dimensional multi-channel ultrasound current source density imaging. IEEE Trans Ultrason Ferroelectr Freq Control 2014;61:420–427.

Wen H, Shah J, Balaban R. Hall effect imaging. IEEE Trans Biomed Eng 1998;45:119–124.

Xu Y, He B. Magnetoacoustic tomography with magnetic induction (MAT-MI). Phys Med Biol 2005;50:5175–5187.

Zhang H, Wang LV. Acousto-electric tomography. In: Oraevsky AA, Wang LV, (eds). Photons Plus Ultrasound: Imaging and Sensing 145. Proc SPIE 2004;5320;. p. 145–149.

APPENDIX

From the basic principles of the AE effect, the resistance R of a tissue slab under the modulation of ultrasound is related to the ultrasound pressure as in the equation

$$R = \rho_0(1-K_I\Delta P)\frac{l}{A} = (1-K_I\Delta P)R_0 = (1+x)R_0 \tag{A1}$$

where l and A are the length and cross-sectional area of a slab $x = -K_I\Delta P$, respectively, and R_0 is the static resistance without pressure applied.

In Figure 1c and d, the voltage source applied on the two ends of the tissue slabs is V, so the static currents in two tissue slabs with resistances R_1 and R_2 are $I_1 = V/R_1$ and $I_2 = V/R_2$, respectively. The voltage drops, V_α, $V_{1-\alpha}$, V_β and $V_{1-\alpha}$, caused by the ultrasound modulation on segments αR_1, $(1-\alpha)R_1$, βR_2 and $(1-\beta)R_2$ can be expressed as

$$V_\alpha = \frac{(1+x)\alpha R_1}{(1+x)\alpha R_1+(1-\alpha)R_1}V = \frac{(1+x)\alpha}{x\alpha+1}V \tag{A2}$$

$$V_{1-\alpha} = \frac{(1+x)(1-\alpha)R_1}{(1+x)(1-\alpha)R_1+\alpha R_1}V = \frac{(1+x)(1-\alpha)}{1+x(1-\alpha)}V \tag{A3}$$

$$V_\beta = \frac{(1+x)\beta R_2}{(1+x)\beta R_2+(1-\beta)R_2}V = \frac{(1+x)\beta}{x\beta+1}V \tag{A4}$$

$$V_{1-\beta} = \frac{(1+x)(1-\beta)R_1}{(1+x)(1-\beta)R_1+\beta R_1}V = \frac{(1+x)(1-\beta)}{1+x(1-\beta)}V \tag{A5}$$

From (A2)–(A5), when $\alpha = \beta = 0.5$, the four voltage drops have the same value; therefore, the optimal position of the detecting electrode on each branch is at the midpoint.

When the ultrasound beam focuses on the left part of the slabs (Fig. 1a), αR_1 and βR_2 are modulated by pressure when at the arrival time of the pulse. The signals detected by the differential amplifiers using the first circuit (Fig. 1c) and second circuit (Fig. 1d) are U_1 and U_2:

$$U_1 = V_\alpha - V_\beta \tag{A6}$$

$$U_2 = V_\alpha - (V - V_\beta) \tag{A7}$$

To reconstruct voltage drops on the segments αR_1 and βR_2, the two signals U_1 and U_2 detected by the two circuits are added and subtracted as in

$$\frac{U_1+U_2}{2} = V_\alpha - \frac{V}{2},\ \frac{U_1-U_2}{2} = -V_\beta + \frac{V}{2} \tag{A8}$$

If the A-line is filtered by a bandpass filter with the same center frequency of the ultrasound, then

$$\frac{u_1+u_2}{2} = v_\alpha,\ \frac{u_1-u_2}{2} = -v_\beta \tag{A9}$$

where u_1, u_2, v_α and v_β are the AC components of U_1, U_2, V_α and V_β, respectively. As α and β are independent to each other, v_α and v_β are two independent components.

When ultrasound is positioned on the right (Fig. 1a), then $(1-\alpha)R_1$ and $(1-\beta)R_2$ will be modulated by pressure when the pulse propagates to reach them. The signals detected by the differential amplifiers using the first circuit (Fig. 1c) and second circuit (Fig. 1d) are U_1 and U_2:

$$U_1 = (V - V_{1-\alpha}) - (V - V_{1-\beta}) = -V_{1-\alpha} + V_{1-\beta} \tag{A10}$$

$$U_2 = (V - V_{1-\alpha}) - V_{1-\beta} = V - V_{1-\alpha} - V_{1-\beta} \tag{A11}$$

To reconstruct the voltage drops on the segments $(1-\alpha)R_1$ and $(1-\beta)R_2$, the two signals U_1 and U_2 detected by two circuits are added and subtracted as in

$$\frac{U_1+U_2}{2} = -V_{1-\alpha} + \frac{V}{2},\ \frac{U_1-U_2}{2} = V_{1-\beta} - \frac{V}{2} \tag{A12}$$

If each A-line is filtered by the bandpass filter, then

$$\frac{u_1+u_2}{2} = -v_{1-\alpha},\ \frac{u_1-u_2}{2} = v_{1-\beta} \tag{A13}$$

where u_1, u_2, $v_{1-\alpha}$ and $v_{1-\beta}$ are the AC components of U_1, U_2, $V_{1-\alpha}$ and $V_{1-\beta}$, respectively. $v_{1-\alpha}$ and $v_{1-\beta}$ are also two independent components.